Origin of Strong Nonlinear Dependence of Fracture (Joint) Spacing on Bed Thickness in Layered Rocks: Mechanical Analysis and Modeling

Alexandre Chemenda, J. Lamarche, Christophe Matonti, L. Bazalgette, P. Richard

Correspondence to:

A. Chemenda,
chem@geoazur.unice.fr

Origin of Strong Nonlinear Dependence of Fracture (Joint) Spacing on Bed Thickness in Layered Rocks: Mechanical Analysis and Modeling

A. I. Chemenda[1] , **J. Lamarche[2]**, **C. Matonti[1]** , **L. Bazalgette[3]**, and **P. Richard[4]**

[1]Université Côte d'Azur, Observatoire de la Côte d'Azur, CNRS, IRD, Géoazur, Valbonne, France, [2]Aix-Marseille University, CNRS, IRD, INRAE, Collège France, CEREGE, Aix-en-Provence, France, [3]Petroleum Development Oman (PDO), Field Development Centre, Mina al Fahal, Oman, [4]Shell Global Solutions International BV, Rijswijk, The Netherlands

Abstract Fracturing (jointing) affects large volumes of rocks and strongly impacts their mechanical stability and permeability. In layered sedimentary basins, the fractures typically form subparallel sets with different fracture spacing S. This parameter has been extensively studied both in the field and in mechanical models in relation to the thickness T of the fractured layers. A linear relation was suggested by most studies. A few geological investigations involving wide ranges of T values have shown that the $T(S)$ relation is generally strongly nonlinear and that in thick beds ($T > \sim 1.5$ m), S practically does not depend on T. The origin of this relation remained hitherto unexplained. Here we obtained such a relation in 2-D finite-difference models of 3-layer sedimentary sequences where layers interact through the interfaces of strength R. The middle layer has elastoplastic properties with coupled tensile and shear failure mechanisms. The number of fractures forming in this layer increases under horizontal extension to a saturation value S depending on R. At $T < \sim 0.5$ m, the increase of S with T is near-linear. At ~ 1 m $< T < 2$ m, it is strongly nonlinear; and S changes little at larger T where S is more than certain value S_{cr}. The increase of ratio $D = T/S$ with T is, on the contrary, close to linear. This behavior is explained by the fact that for $D > \sim 2$, the stress state in the upper and lower horizons of the middle layer between fractures spaced $2S_{cr}$ apart is practically independent of T.

1. Introduction

Fractures are ubiquitous in the Earth's crust. They strongly impact the mechanical stability, strength, and permeability of geological structures or rock masses and thereby play an essential role in many societally important processes in the upper crust as well as in the management of subsurface engineering operations. The most common are the so-called opening mode (extension or tensile/tension) fractures or joints. They often form regular sets of parallel, orthogonal, or more complex fracture networks. Because of their practical importance, notably for the oil and gas industry, joints have been extensively studied for more than a century (e.g., Pollard & Aydin, 1988), mostly in sedimentary basins composed of alternating layers with contrasted lithology (Figures 1a–1c) and hence mechanical properties. Particular attention has been paid to the joint spacing S or the ratio D of the fractured layer thickness T to S ($D=T/S$). The main practical aim has been to predict the fracture spacing at depth from bed thickness. The spacing of natural fractures cannot be observed directly in the subsurface, whereas the bed thickness can be defined from petrophysical well data or core analysis. These works stimulated research in rock/fracture mechanics and modeling (Bai & Pollard, 2000; Cherepanov, 1997; Gross et al., 1995; Guo et al., 2017; Hobbs, 1967; Ji et al., 1998; Li et al., 2012; Price, 1966; Schöpfer et al., 2011). Geological observations (e.g., Bogdanov, 1947; Engelder et al., 1997; Gross, 1993; Huang & Angelier, 1989; Ji et al., 1998; Narr & Suppe, 1991), mechanical analysis, and modeling (Bai & Pollard, 2000; Cherepanov, 1997; Gross et al., 1995; Hobbs, 1967; Ji et al., 1998; ; Li et al., 2012; Price, 1966) have shown that values of T and S are linearly related and ratio D commonly varies in a small range around 1. All this has been explained within the framework of a simple elastic analysis of the mechanical interaction between the layers (e.g., Bai & Pollard, 2000; Gross et al., 1995; Jain et al., 2007; Ji et al., 1998). However, several field studies revealed much higher D values and strongly nonlinear $T(S)$ relations (Figure 1d) when sedimentary beds with large T ($T>1-2$ m) like in Figure 1c were included in the analysis (Ladeira & Price, 1981; McQuillan, 1973; Sagy & Reches, 2006). Based on the extensive data sets
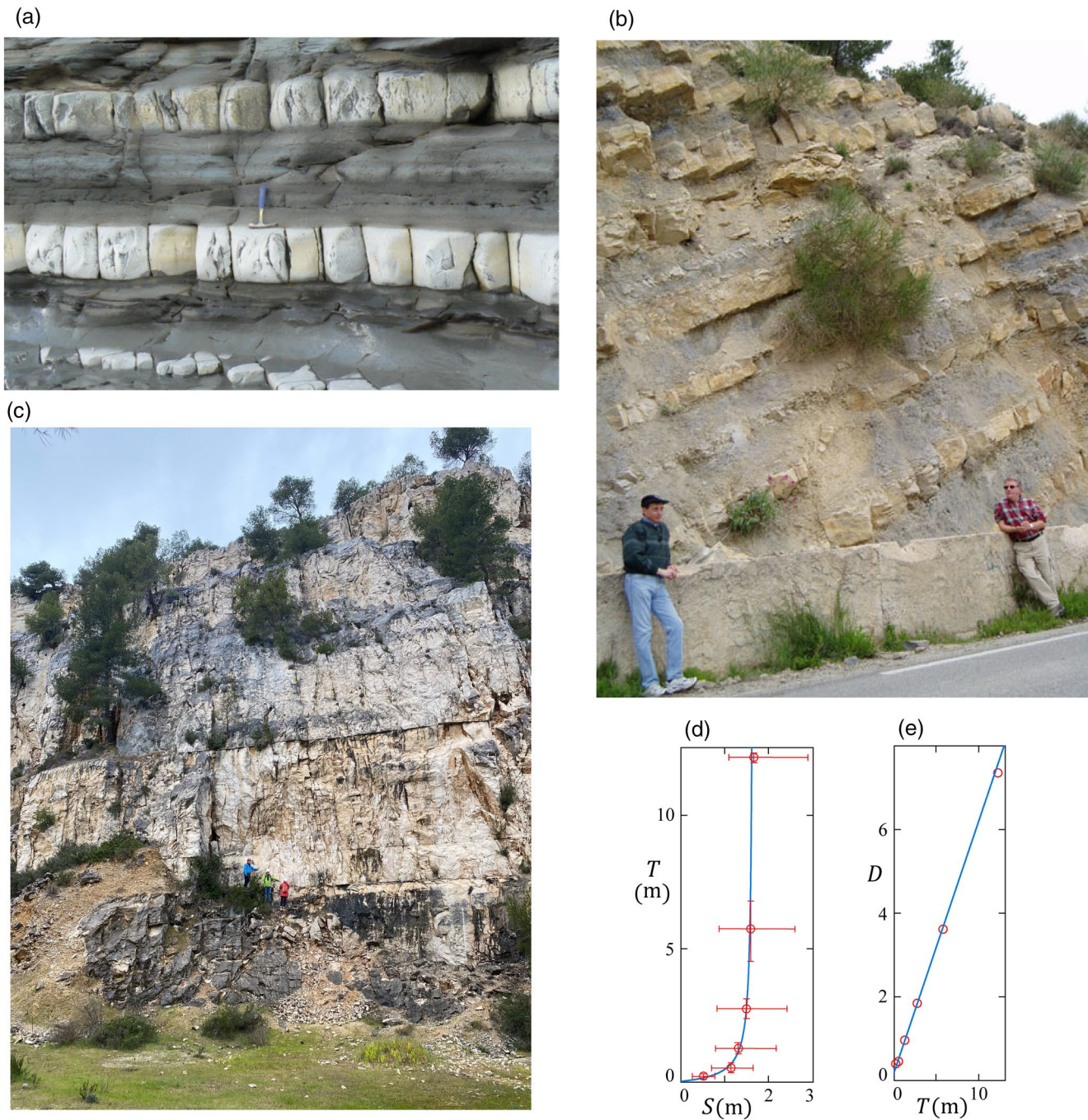
Figure 1. (a–c) Field examples of layered and fractured sedimentary rocks. (a) Alternating incompetent (mudrocks) and fractured competent (limestone) layers in Lilstock Bay, Somerset, UK (rock hammer for scale) from Schöpfer et al. (2011). (b) Marly shale and fractured limestone layers of different thicknesses in Aalenian rocks of Sainte Beaume Range, Provence, SE France. (c) Thick densely fractured (with $D \gg 1$) (Lamarche et al., 2012) Urgonian limestone layers; Cassis, Provence, SE France. (d) Field measurements of fracture spacing S in Asmari limestone layers in major folds in Zagros by McQuillan (1973) in the presentation of Ladeira and Price (1981). There are six data groups corresponding to different ranges of layer thicknesses T shown by vertical error bars. Ranges of S variation are also shown for each group with average values indicated by red circles. The blue line is the plot of function $T=bS/(1-aS)$, which fits the modeling results reported here and is discussed below. (e) The same points as in (d) but plotted in the coordinates (D, T), where $D=T/S$. The blue line is a plot of $D=aT+b$, where coefficients a and b are the same as in (d): a=0.61 m^{-1} and b=0.18 m.

Figure 2. Setup of 3-layer 2-D numerical models. (a) Series of alternating incompetent (pink) and competent (blue) layers. (b) An elementary (repeating) element of this series which corresponds to the complete three-layer modeling setup. (c) A half-symmetry modeling setup, with thicknesses of layers 1 and 2 being $T_1/2$ a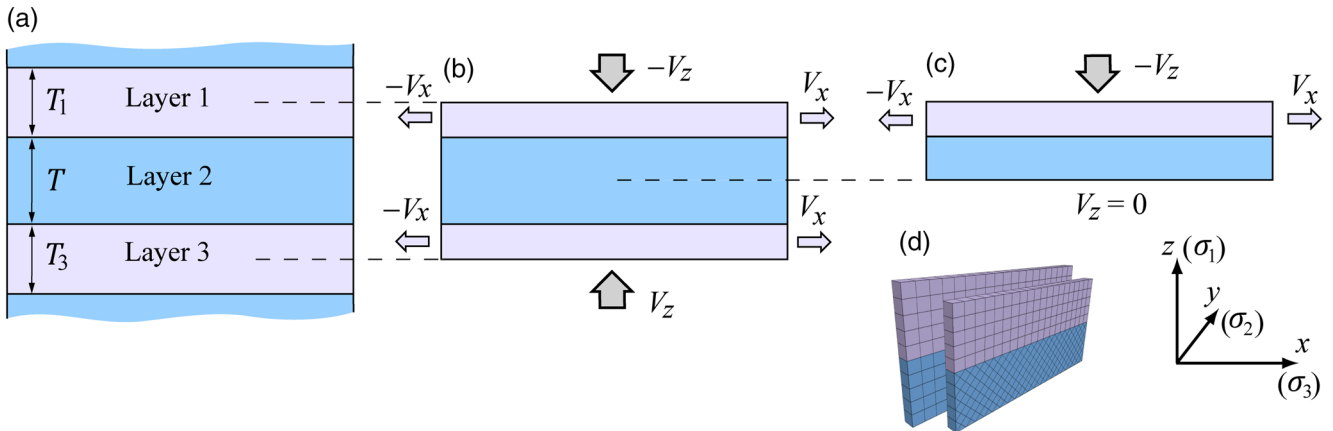nd $T/2$, respectively. (d) The attached two layers of the grid used to reduce the grid anisotropy that can influence the strain localization. V_x and V_z are the velocities applied in the corresponding directions to layers 1 and 3. V_x causes deformation and fracturing of layer 2 and V_z is to maintain constant average vertical stress at the horizontal model boundaries. The y-normal model boundaries are fixed in the y-direction. The models are prestressed in the y- and z-directions as described in the text. Layers 1 and 3 are purely elastic and layer 2 is elastoplastic.

from different tectonic settings, McQuillan (1973) and Ladeira and Price (1981) concluded that the $T(S)$ relation is quasilinear with a relatively shallow slope D of the $T(S)$ curve only up to a certain T value of about 1.5 m on average. At larger T, S increases very slowly with T (Figure 1d) or does not increase at all.

Ladeira and Price (1981) and Price and Cosgrove (1990) suggested that at large T, the fracture mechanism is not directly related to the layer interaction and is due to the elevated pore pressure that exceeds the compressive least stress and allows the tensile failure. The near-constant S was explained by the fact the fluid pressure drops in the vicinity of the forming fracture. The formation of the next fracture could be possible only at a certain distance (constant for given conditions) where the fluid pressure is not affected by the formation of the previous fracture. Other researchers did not take up this conceptual scenario. Neither were any other mechanisms proposed to our knowledge, and most of the studies were focused on the sedimentary sequences characterized by T values limited to several decimeters. Here we reproduce dependencies $T(S)$ and $D(T)$ like those in Figures 1d and 1e in three-layer numerical models and show that they are entirely (or at least mostly) due to the mechanical interaction between the layers. This study is based on theoretical and numerical models developed by Chemenda (2019). They are summarized in the next two sections where the modifications made for this study are shown.

2. Constitutive Model

As in the previous numerical modeling studies (e.g., Bai & Pollard, 2000; Gross et al., 1995; Schöpfer et al., 2011), we investigate here three-layer 2-D models (Figure 2). Only the central layer (layer 2) can fracture, whereas two others (layer 1 and 3) are purely elastic. The constitutive model for layer 2 includes the following composite yield function

$$F = \begin{cases} F_t = \sigma_t + \sigma_3 & if \ \sigma_1 \leq \sigma_{\text{int}} \\ \\ F_s = \alpha_c \sigma_3 + \sigma_c - \sigma_1 \ if \ \sigma_1 > \sigma_{\text{int}} \end{cases} \quad (1)$$

where F_t and F_s are the yield functions for the tensile and shear failure mechanisms, respectively; σ_t and σ_c are the tensile and unconfined compression strengths, respectively; σ_{int} is the abscissa of the intersection point of the envelopes $F_t = 0$ and $F_s = 0$ in the (σ_1, σ_3) space. We use a rock mechanics convention for

stresses: $\sigma_1 \geq \sigma_2 \geq \sigma_3$; the compressive stress is positive; all stresses are effective. The parameters σ_t, σ_c, and σ_{int} are functions of the accumulated inelastic volume strain ε^p

$$\begin{aligned} \sigma_t\left(\varepsilon^p\right) = \sigma_t^0 \kappa\left(\varepsilon^p\right), \sigma_c\left(\varepsilon^p\right) = \sigma_c^0 k\left(\varepsilon^p\right), \sigma_{\text{int}}^0\left(\varepsilon^p\right) = \sigma_{\text{int}}^0\left(\varepsilon^p\right) \quad if \ \varepsilon^p \leq \varepsilon^0 \\ \sigma_t\left(\varepsilon^p\right) = \sigma_c\left(\varepsilon^p\right) = \sigma_{\text{int}}\left(\varepsilon^p\right) = 0 \quad if \ \varepsilon^p > \varepsilon^0 \end{aligned} \tag{2}$$

where ε^0 is the ε^p value at which σ_t and σ_c reach zero during failure; $\kappa\left(\varepsilon^p\right) = 1 - \varepsilon^p / \varepsilon^0$; σ_t^0, σ_c^0, and σ_{int}^0 are the initial (at $\varepsilon^p = 0$) values of σ_t, σ_c, and σ_{int}; α_c is the dimensionless material (friction) parameter defined from the experimental data and related to the Coulomb internal friction angle φ as

$$\alpha_c = \frac{1 + \sin\left(\varphi\right)}{1 - \sin\left(\varphi\right)}. \tag{3}$$

A 3-D plot of the defined yield function (1 and 2) is given in Chemenda (2019).

Considering (1), the plastic potential function Φ can be written

$$\Phi = \begin{cases} \Phi_t = \sigma_3 \quad if \ \sigma_1 \leq \sigma_{\text{int}} \\ \\ \Phi_s = \beta_c \sigma_3 - \sigma_1 \ if \ \sigma_1 > \sigma_{\text{int}} \end{cases} \tag{4}$$

where Φ_t and Φ_s are the plastic potentials for the tensile and shear failure mechanisms, respectively; β_c is the material coefficient. Chemenda (2019) assumed, for simplicity, complete associativity (or normality) of the flow rule, $\Phi = F$, meaning that $\beta_c = \alpha_c = $ constant. β_c defines the dilatancy factor β, which is known, however, to depend on inelastic strain (e.g., Mas & Chemenda, 2015; Sulem et al., 1999). Here we consider this dependence as described below.

The dilatancy factor is usually defined as $\beta = d\varepsilon^p / d\overline{\gamma}^p$, where $d\overline{\gamma}^p$ is the increment of inelastic equivalent shear strain

$$d\overline{\gamma}^p = \sqrt{2\left[\left(d\varepsilon_1^p - d\varepsilon_2^p\right)^2 + \left(d\varepsilon_1^p - d\varepsilon_3^p\right)^2 + \left(d\varepsilon_2^p - d\varepsilon_3^p\right)^2\right] / 3} \tag{5}$$

(superscript "p" stands for plastic or inelastic). For the tensile failure/damage mechanism, $\beta = \sqrt{3} / 2$ (Chemenda, 2019), and for the shear mechanism, it is defined by β_c

$$\beta = \frac{\sqrt{3}\left(\beta_c - 1\right)}{2\sqrt{\beta_c^2 + \beta_c + 1)}}. \tag{6}$$

as can be obtained from (4, 5) and the flow rule

$$d\epsilon_j^p = d\lambda \frac{\partial \Phi_s}{\partial \sigma_j}, \tag{7}$$

where $d\lambda$ is the nonzero scalar function ($d\lambda$ is different for the different failure mechanisms introduced), $j = 1, 2, 3$.

β in (6) reaches zero (no inelastic volume change) at $\beta_c = 1$. The simplest, therefore, would be to assume that β_c linearly decreases with ε^p from the initial value β_c^0 to 1. It is logical to relate the end of the inelastic volume change to the complete material failure when both σ_t and σ_c become zero. In this case, β_c reaches 1 at $\varepsilon^p = \varepsilon^0$ and is expressed as

$$\beta_c = \begin{cases} \beta_c^0 + \left(1 - \beta_c^0\right)\varepsilon^p \,/\, \varepsilon^0 & if \ \varepsilon^p \le \varepsilon^0 \\ \\ 1 & if \ \varepsilon^p > \varepsilon^0 \end{cases} \tag{8}$$

The pattern of the fractures generated in the models with $\beta_c^0 = \alpha_c$, $\beta_c^0 = 1$ ($\beta = 0$) as well as $\beta_c = \alpha_c = $ const is the same. Some difference was observed only in the speed of fracture propagation, which is discussed below. Here we present modeling results for β_c defined in (8) with $\beta_c = \beta_c^0 = 1$.

To deal with the mesh dependence of the modeling results, the mesh (numerical zone) size Δz is included in the constitutive formulation by relating ε^0 and Δz (Chemenda, 2019)

$$\varepsilon^0 = \tilde{\varepsilon}^0\left(\frac{C}{\Delta z}\right) \tag{9}$$

where C is a constant coefficient, and $\tilde{\varepsilon}^0$ is equal to ε^0 when $\Delta z = C$. This is similar to the approach applied by Bažant & Oh (1983) in fracture modeling. Including Equation 9 into constitutive model is necessary because joints are not treated here as clear-cut fractures but as more complex objects evolving from pure dilation deformation localization bands, as is suggested by the experimental (Chemenda et al., 2011a) and field (Chemenda et al., 2011b) data. The deformation banding results from a constitutive or material instability captured by finite-element and finite-difference numerical models. This process, however, is known to be mesh-dependent. Relation (9) allows to strongly reduce this dependency, as is shown in Chemenda (2019) and below in this study. The physical sense of this relation can be understood from the following simple analysis. After the initiation, the dilation band borders move apart during extension at a distance Δd, which is accompanied by progressive damage (inelastic deformation) of the material within the band until complete failure or fracture formation. To obtain the same (physically similar) banding (fracture) process in the models with different resolutions (different Δz), the rate of inelastic energy dissipation W within the band during its extension in the models should be the same for different Δz. During the tensile failure, only σ_3-parallel component of inelastic strain is nonzero and is equal to ε^p as follows from (4 and 7). This strain occurs under σ_3 equal to $\sigma_t\left(\varepsilon^p\right)$ defined in (2). Assuming that inelastic straining within the band is uniform, that the band width d_0 is proportional to Δz ($d_0 \sim \Delta z$), and $\varepsilon^p = \Delta d \,/\, d_0 \ \sim \Delta d \,/\, \Delta z$, the energy dissipation rate W per unit height and thickness of the band can be written as

$$W = \frac{d_0}{\Delta d}\int_0^{\varepsilon^p} \sigma_t\left(\varepsilon^p\right)d\varepsilon^p \ \sim \ \frac{\Delta z}{\Delta d}\int_0^{\Delta d}\sigma_t\left(\frac{\Delta d}{\Delta z}\right)\frac{\mathrm{d}\left(\Delta d\right)}{\Delta z} = \sigma_t^0\left[1 - \frac{\Delta d}{2\Delta z\varepsilon^0}\right] \tag{10}$$

It is seen that W will be constant for a given Δd when $\Delta z\varepsilon^0 = $ constant. This condition is equivalent to (9), implying that the reduction of σ_t within the band for a given Δd is independent of Δz. This means that the hardening modulus should decrease with the increase of Δz, which is discussed below. The energy dissipation during the complete material failure within the band (the fracture energy)

$$W_f = d_0\int_0^{\varepsilon^0}\sigma_t\left(\varepsilon^p\right)d\varepsilon^p = \frac{1}{2}d_0\sigma_t^0\varepsilon^0 \ \sim \ C\sigma_t^0\tilde{\varepsilon}^0$$

is also Δz-independent. Therefore, W_f does not vanish when $\Delta z \to 0$ and the structural load-deformation response is the same for different Δz (provided that Δz is much smaller than the model size).

The d_0 value in the models presented below is ~1 cm, which is a few orders of magnitude larger than in reality (in rocks). Therefore, the ε^0 value in these models cannot be equal to that for real rocks and must depend on Δz as indicated above (Equation 9). d_0 depends on (is proportional to) Δz as well. This dependence can be reduced in the models using regularization procedures (see the related discussion and references in Chemenda (2019)). They allow avoiding the ill-posedness of the initial value problem during deformation localization but do not fundamentally affect the modeling results, as can be seen in Figure 2 of Prevost and Loret (1990).

We have implemented the formulated constitutive model into the finite-difference dynamic time-matching explicit code FLAC3D (Itasca, 2013), used in a quasistatic mode (i.e., steady-state solution of a fully dynamic problem is obtained by a dynamic relaxation method). The elastic behavior is modeled by Hooke's equations.

3. Modeling Setup

A three-layer model is subjected to the velocity boundary conditions as shown in Figure 2b and is prestressed to the initial stresses σ_{zz}^{ini} and σ_{yy}^{ini} in the z- and y-directions, respectively. Layers 1 and 3 are subjected to the horizontal extension, which creates shear stresses at the layer interfaces driving the extension and fracturing of the central layer 2. This layer has free vertical boundaries that correspond, therefore, to preexisting fractures. This means that we do not consider models that are uniformly stressed and strained until fracturing that would correspond to infinitely long unfractured layers. Instead, we model a layer segment limited by two already formed (preexisting) fractures. It will be shown below that the modeling results obtained with these two types of boundary conditions do not differ significantly. To maintain a quasistatic deformation regime, velocity V_x applied to layers 1 and 3 is servo-controlled and varies between ~0 and 1×10^{-7} m/s.

Following Chemenda (2019), the models have two attached grid layers in the y-direction with grid elements having the different regular geometry for layer 2, Figure 2d (the attach logic is given in Itasca, 2013). This considerably reduces the grid anisotropy that may affect strain localization, particularly when the orientation of the fracture/band changes during its propagation.

The horizontal extension applied to the model causes its vertical shortening. To maintain the average vertical stress constant and equal to σ_{zz}^{ini}, we apply servo-controlled vertical velocities V_z to the horizontal boundaries of the models (Figure 2b) that vary between ~0 and 1×10^{-9} m/s. This stress corresponds to a constant effective lithostatic stress produced by the overlying layers (that are not modeled). It could be applied directly to the top and bottom of the model, as has been done in Chemenda (2019). Such a constant-stress boundary condition corresponds to a zero stiffness of the overlying layers. The velocity boundary condition used here corresponds to the infinite stiffness. The reality lies between these two end-member cases. Although the modeling results obtained for these two cases do not differ much (as shown below), the vertical velocity boundary conditions appear to be more realistic.

Figure 2b shows the complete modeled structure, but to reduce the calculation time, most of the simulations have been carried out with the half-symmetry models in Figure 2c. The layers are connected by frictional and cohesive interfaces whose shear strength τ_0^i is defined by the interface friction coefficient μ^i and cohesion c^i

$$\tau_0^i = \mu^i \sigma_n + c^i \tag{11}$$

where σ_n is the effective normal to interface stress, which is equal to the vertical normal stress σ_{zz}. The normal (k_n) and shear (k_s) stiffnesses of the interfaces are set to (Itasca, 2013)

$$k_n = k_s = 10\max\left[\frac{E(\nu - 1)}{(\nu + 1)(2\nu - 1)\Delta z}\right] \tag{12}$$

where E and ν are Young's modulus and Poisson's ratio; "max" means that the maximum value over all zones adjacent to the interface is to be used.

3.1. Model Parameter Values

We assume that alternating limestone and shale/marl layers of a thickness of a few tens of centimeters (Figures 1a and 1b) are representative of many sedimentary basins. It is much more difficult to define the layers' mechanical parameters, even of such widely measured and used ones as elastic moduli.

The available values of these moduli and, to a higher degree, of the strength parameters vary in very wide ranges for both limestones and shales (as well as for other rocks). Therefore, it is even difficult to find out which rock type is stiffer or stronger (e.g., Chang et al., 2006; Colmenares & Zoback, 2002; Hoek & Martin, 2014; Mohammed & Mahmood, 2021; Parent et al., 2015; Rybacki et al., 2016; Shao et al., 2019; Vajdova et al., 2004; Xu et al., 2016). The data from these papers suggest the following approximate ranges of parameters for limestones: E=(15−90) GPa, $\nu = 0.17 − 0.33$, $\sigma_c = (20 − 200)$ MPa, $\sigma_t = (2 − 20)$ MPa, $\varphi = 20 − 40°$ where E and ν are Young's modulus and Poisson's ratio, respectively. For shales, the elastic moduli are $E = (20 − 90)$ GPa; $\nu = 0.25 − 0.4$. All values are defined from experimental testing. One can suppose that these values will be much smaller at the geological time- and spatial-scales, particularly for incompletely lithified rocks fractured during burial. Therefore, the values (first of all those for the strengths) chosen for the modeling in this work are closer to the lower limits of the indicated ranges: $E = 20$ GPa; $\nu = 0.25$; $\sigma_c = 60$ MPa, $\sigma_t = 7$ MPa, $\varphi = 30°$. These parameter values are applied for the limestone (or competent) layers. The same elastic moduli are used for the shale (incompetent) layers. No other mechanical parameters for shale are needed as it is assumed to behave elastically. This is obviously a simplification as shales can relatively easily creep, although there is a correlation between creep compliance and Young's modulus (e.g., Sone & Zoback, 2013). It should be noted that several models were run with different elastic moduli. A reasonable estimation for density ρ of both limestone and shale layers is =2,600 kg/m^3.

The reference thickness of all the layers in our models is T_1=T_2=T=20 cm (see Figure 2a for definitions); it becomes 10 cm for the half-symmetry setup in Figure 2c. Two more parameters $\tilde{\varepsilon}^0$ and C (Equation 9) are needed to characterize the limestone layer. They are not known at all for rocks. Parameter $\tilde{\varepsilon}^0$ is a reference inelastic strain at complete failure, ideally to be defined from the experimental data and hence characterizing properties of real material. Using $\varepsilon^0 = \tilde{\varepsilon}^0$ in the models would require that the fracture (band) thickness in the models is equal to that in real rocks where it is of several grain sizes. This means that Δz should be smaller than the grain size, which is impossible when addressing most of the real-life geological problems. Therefore, we must use larger Δz, and to obtain the same (similar) fracture process and fracture pattern as in real material, ε^0 for the modeling should be defined by Equation 9. Coefficient C corresponds to the reference mesh size and can be evaluated by comparing fracture patterns in numerical models and the experimental tests conducted under similar conditions. That is what has been done in Chemenda (2019) based on the experimental models of synthetic rock analog material GRAM. Values $\tilde{\varepsilon}^0_{GR} = 10^{-3}$ and C=C_{GR}=2.5×10^{-4} m were assumed for GRAM models (here and below, subscript "GR" stands for GRAM). The models in this study are much larger, stiffer, and stronger. Therefore, C_{GR} value cannot be used and should be upscaled. We do it below using the normalized hardening modulus h for the tensile failure

$$h = \frac{1}{G}\frac{\partial \sigma_t(\epsilon^p)}{\partial \epsilon^p} = -\frac{\sigma_t^0 \Delta z}{GC\tilde{\varepsilon}^0},$$

(13)

which is critical for deformation localization (bifurcation) phenomenon, and defines its onset (Rice, 1976; Rudnicki & Rice, 1975), the rate of the formation and spacing of the initiating deformation bands (Chemenda, 2007, 2009), as well as the brittleness/ductility of the fracture process. This dimensionless parameter should be considered a similarity criterion (i.e., be constant) when we change the scale of a phenomenon but want to keep its physics (ensure physical similarity). Condition h=constant results in the following relation

$$C = C_{GR}\frac{\eta_s \eta_\sigma}{\eta_G \eta_\varepsilon}$$

(14)

where $\eta_s = T / T_{GR}, \eta_G = G / G_{GR}, \eta_\sigma = \sigma_t^0 / \sigma_{tGR}^0, \eta_\varepsilon = \tilde{\varepsilon}^0 / \tilde{\varepsilon}^0_{GR}$; T_{GR}=1 cm, G_{GR}=0.67 GPa, and $\sigma_t^0 = 0.07$ MPa (Chemenda, 2019). It is assumed here that the numerical resolution of small and large models in terms of geometrical sizes is the same or that T/T_{GR}=$\Delta z/\Delta z_{GR}$. Value 10^{-3} used for $\tilde{\varepsilon}^0_{GR}$ seems to be also applicable to rocks and thus can be assumed for $\tilde{\varepsilon}^0$. Therefore, $\eta_\varepsilon = 1$ and C defined by (14) should be

about two orders of magnitude larger than C_{GR}. We assume $C = 0.1$ m, but also show modeling results for C one order of magnitude smaller and larger. In should be noted, that what matters is not merely the C value but the value of the product $C\tilde{\varepsilon}^0$, Equation 9. Therefore, one can vary $\tilde{\varepsilon}^0$ instead of C, which has been done in (Chemenda, 2019) where $\tilde{\varepsilon}^0$ was varied in wide limits, $5 \times 10^{-4} \leq \tilde{\varepsilon}^0 \leq 5 \times 10^{-2}$, showing the impact of this parameter on fracturing. Note that the increase of the model resolution (reduction of Δz) requires the growth of the negative hardening modulus (Equation 13), which corresponds to a more ductile material response in terms of constitutive description. However, the macro-response of such a model or, more precisely, the fracture process and pattern, will be similar to those in low-resolution models.

For the vertical (lithostatic) stress σ_{zz}^{ini} applied to the models, we assume the value of 10 MPa and for the horizontal stresses, $\sigma_{xx}^{\text{ini}} = 0$ and $\sigma_{yy}^{\text{ini}} = \sigma_{zz}^{\text{ini}} / 2$. As indicated above, all stresses are considered effective. Therefore, assuming that the pore pressure is equal to the hydrostatic pressure, the lithostatic stress σ_{zz}^{ini} is related to the depth z as

$$\sigma_{zz}^{\text{ini}} = \left(\rho - \rho_w\right)gz \tag{15}$$

where $\rho_w = 10^3$ kg/m³ is the water density, and g is the acceleration of gravity. For the chosen value of σ_{zz}^{ini}, z=640 m. The depth of fracture generation in natural sedimentary basins is not well known. It probably varies from a few kilometers (e.g., Fall et al., 2015) to very shallow depths corresponding to the onset of lithification. Early embrittlement processes are common, particularly for carbonates or marly lithology (e.g., La Bruna et al., 2020), allowing fracture generation even in the first few hundreds of meters (e.g., La Bruna et al., 2020; Lavenu & Lamarche, 2018; Lavenu et al., 2013; Matonti et al., 2017). At the early (small-depth) fracturing, σ_t can be much smaller than the assumed value. To have the same (similar) fracturing conditions, σ_{zz}^{ini} and hence z should be reduced proportionally to the σ_t reduction.

Regarding the interface properties, preliminary numerical simulations have shown that what matters in the models is the interface shear strength τ_0^i independently on the values of its friction and cohesion components in Equation 11. Therefore, for simplicity, we set $\mu^i = 0$ and hence τ_0^i is equal to c^i. This parameter is varied in the models, with the reference value being $c^i = \tau_0^i = 2$ MPa.

4. Modeling Results

Since only the central layer (layer 2, Figure 2) can fracture in the models, only this layer is shown below on the model images. We conducted most of the models using the half-symmetry setup in Figure 2c. Only models in Figures 4g and 4h were run using the complete setup in Figure 2b for comparison. The reference parameter values defined above are summarized here: $E = 20$ GPa; $\nu = 0.25$; $\sigma_c^0 = 60$ MPa, $\sigma_t^0 = 7$ MPa, $\alpha_c = 3$, $\beta_c^0 = 1$, $C = 0.1$ m, $c^i = \tau_0^i = 2$ MPa, $k_n = k_s = 9.6 \times 10^{12}$ Pa/m, $\sigma_{zz}^{\text{ini}} = 10$ MPa, $\sigma_{yy}^{\text{ini}} = \sigma_{zz}^{\text{ini}} / 2$, $\sigma_{xx}^{\text{ini}} = 0$, $T_1 = T_3 = T = 20$ cm, $L = 3$ m. The reference grid zone size is Δz=2.5×10⁻² m.

The mechanism driving the deformation and fracturing in the models is a horizontal extension of layers 1 and 3, which is quantified by the nominal normal horizontal strain $\varepsilon_{xx} = -\Delta L / L$, where ΔL is the lengthening of these layers. The fracture pattern is shown in terms of the tensile strength σ_t. When σ_t is equal to its initial value σ_t^0, there is no material damage, and when $\sigma_t = 0$, the material is wholly fractured/failed. The case $0 < \sigma_t < \sigma_t^0$ corresponds to the dilatant damage of the material. Localization of such damage within a narrow band corresponds to dilation or dilatancy band, which can evolve to fracture with the following damage accumulation.

The modeling results are presented in six groups, Group 1 to Group 6 in Figures 3–8, respectively. Models in Groups 1 to 5 differ only by one parameter values: in Group 1 this parameter is ε_{xx}; in Group 2, Δz; in Group 3, c^i; in Group 4, T, and in Group 5, T as well but in one-layer elastic models described later. In
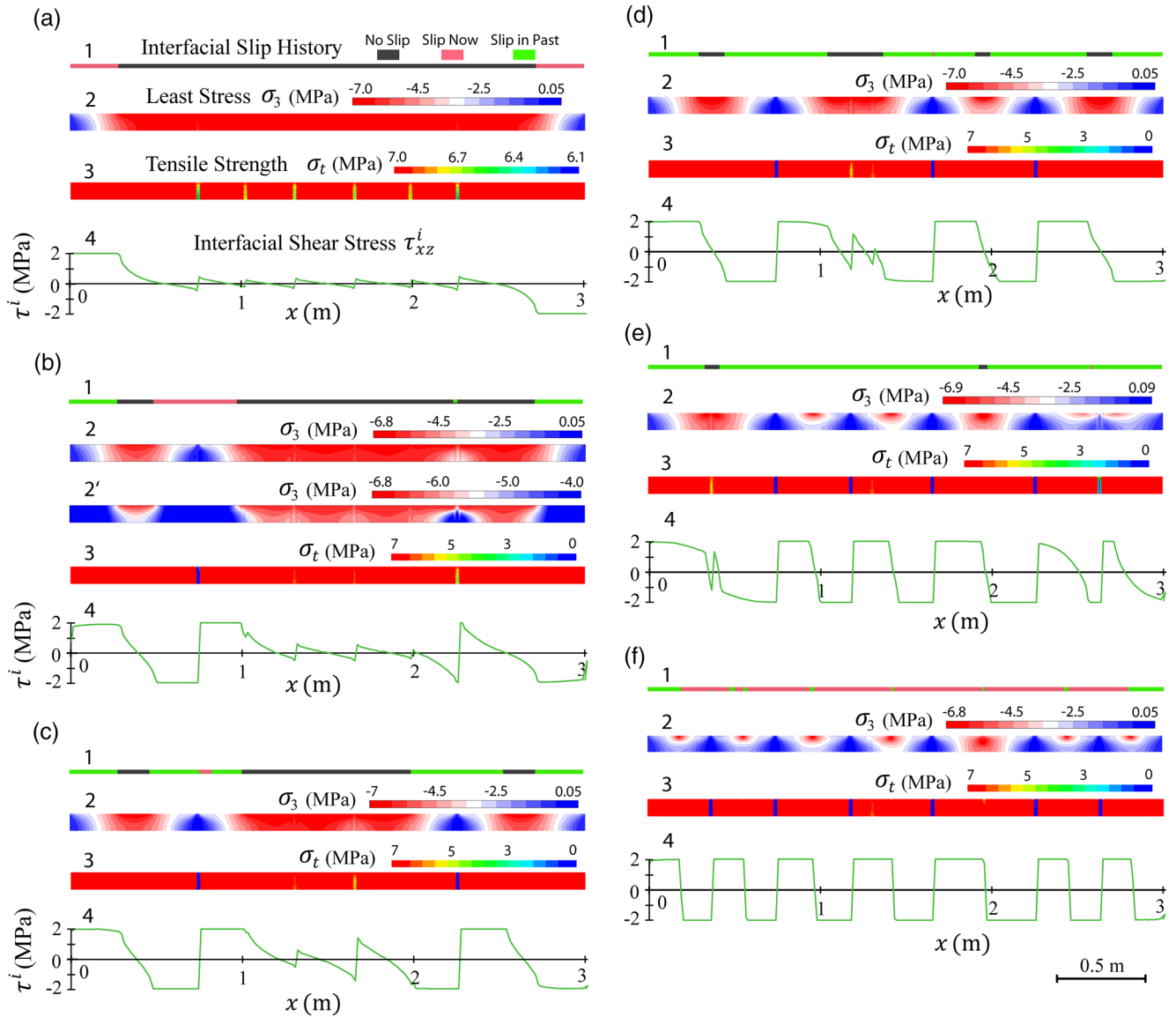
Figure 3. Group 1. (a–f) Evolution of the reference model at different ε_{xx}:
$\varepsilon_{xx} = -3.4 \times 10^{-4}$ in (a); -3.6×10^{-4} in (b); -4.3×10^{-4} in (c); -5.4×10^{-4} in (d); -8.7×10^{-4} in (e); -5×10^{-3} in (f). The interface slip history (1) detailed in (a), the contour plots of σ_3 (2) and σ_t (3), as well as the interface shear stress τ^i (4) along the layer are shown for each fracturing stage. The slip history is presented by a bar with segments of different colors along the layer (its upper interface). The colors correspond to the three possible states at the interface points, as shown in (a1). For example, the bar in (b1) shows that the slip between the layers occurs only along the segment with the center at the left fracture. At the end segments of the layer and in the vicinity of the underdeveloped right fracture (dilation band), slip occurred during the previous deformation stages and was not active at stage (b). Along the remaining part of the interface, the layers did not slip past each other at all (slip occurs there during later deformation stages). (b2') is the same as (b2), but the lower limit of the σ_3 color-scale is reduced to -4 MPa.

Group 6, we present models showing a sensitivity of the modeling results to the boundary conditions and the C value.

Group 1: Figure 3 shows six stages (from a to f) of the evolution of fracture pattern (3 in the figure), the least stress σ_3 (2), the interface shear stress τ^i (4) along the layer, and the interface slip history (1) in the reference model (having the reference parameter values). The initial elastic and nonlocalized inelastic loading stages are omitted, and the first stage shown in (a) corresponds to the formation of a set of dilation bands (Figure 3a3) that are marked by the steps in the $\tau^i(x)$ curve in Figure 3a4 (positive τ^i is oriented to the left and negative, to the right). One can see that although the minimum σ_t value is less than $\sigma_t^0 = 7$ MPa, it is
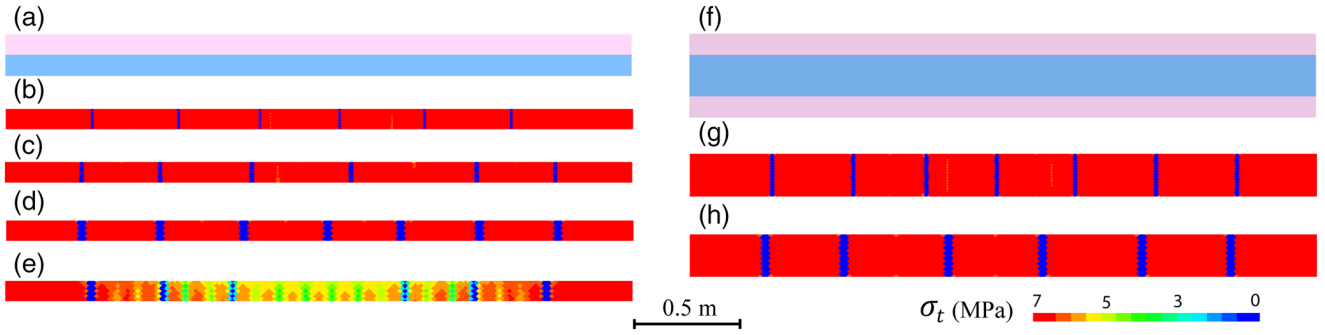
Figure 4. Group 2. Fracture patterns in the models deformed with the half-symmetry (b–e) and complete (g–h) modeling setups shown in (a) and (f), respectively. All models have reference parameters except for the grid zone size Δz, which is 2.5×10^{-2} m in (d, e, and h); 1.125×10^{-2} m in (c) and (g), and 6.25×10^{-3}m in (b). The models were run to $\varepsilon_{xx} = -5 \times 10^{-3}$. In the model in (e), ε^0 was not defined from Equation 9 but set to the same value as in the model in (b), $\varepsilon^0 = 1.6 \times 10^{-2}$.

far from zero at this stage. The σ_3 field is very heterogeneous near the ends of the layer corresponding to stress shadows produced by the preexisting fractures (corresponding to the vertical boundaries of the layer) and is relatively uniform and close to $\sigma_3 = -\sigma_t^0$ in its central part (Figure 3a2). In fact, there is a reduction in $|\sigma_3|$, but it is too small to be seen in this figure; it is seen in Figure 2b2'. The slip at the interface occurs only at the end segments of the layer (Figure 3a1) where τ^i has reached the interface shear strength $\tau_0^i = 2$ MPa (Figure 3a4).

In Figure 3b, one fracture in the left part of the model is wholly formed, and one dilation band, located symmetrically in the right part of the model underwent significant evolution and is seen on the σ_3 plot in b2. Other dilation bands formed at stage **a** are not visible on this plot, but they are seen as 'weak stress
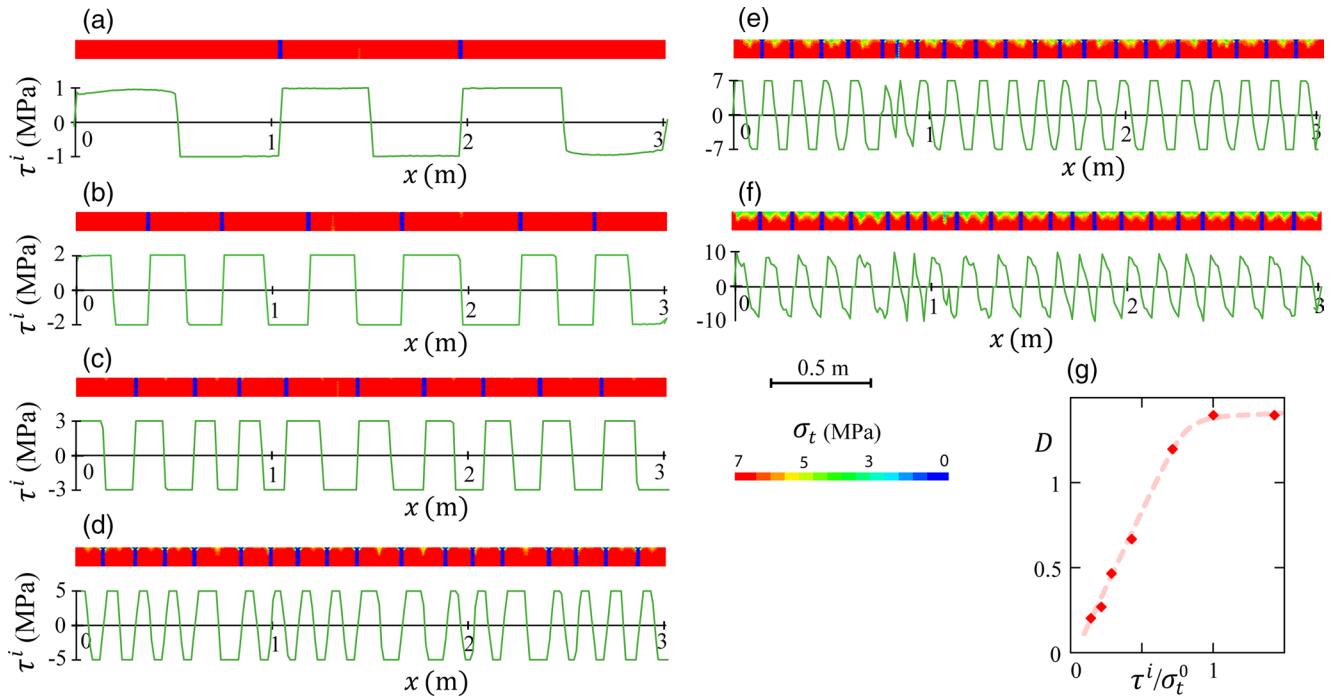

Figure 5. Group 3. (a–f) Fracture patterns and the interface shear stress τ^i between layers 1 and 2 in the reference models with different interface shear strength τ_0^i. The models are shown for $\varepsilon_{xx} = -5 \times 10^{-3}$, but the fracture patterns presented were formed at lower ε_{xx}: -4.6×10^{-4} for $\tau_0^i = 1$ MPa (a); -1×10^{-3} for $\tau_0^i = 2$ MPa (b); -2×10^{-3} for $\tau_0^i = 3$ MPa (c); 3.6×10^{-3} for $\tau_0^i = 5$ MPa (d); -4.1×10^{-3} for $\tau_0^i = 7$ MPa (e); -4.2×10^{-3} for $\tau_0^i = 10$ MPa (f). (g) Ratio D in these and other models plotted versus ratio τ^i / σ_t^0.
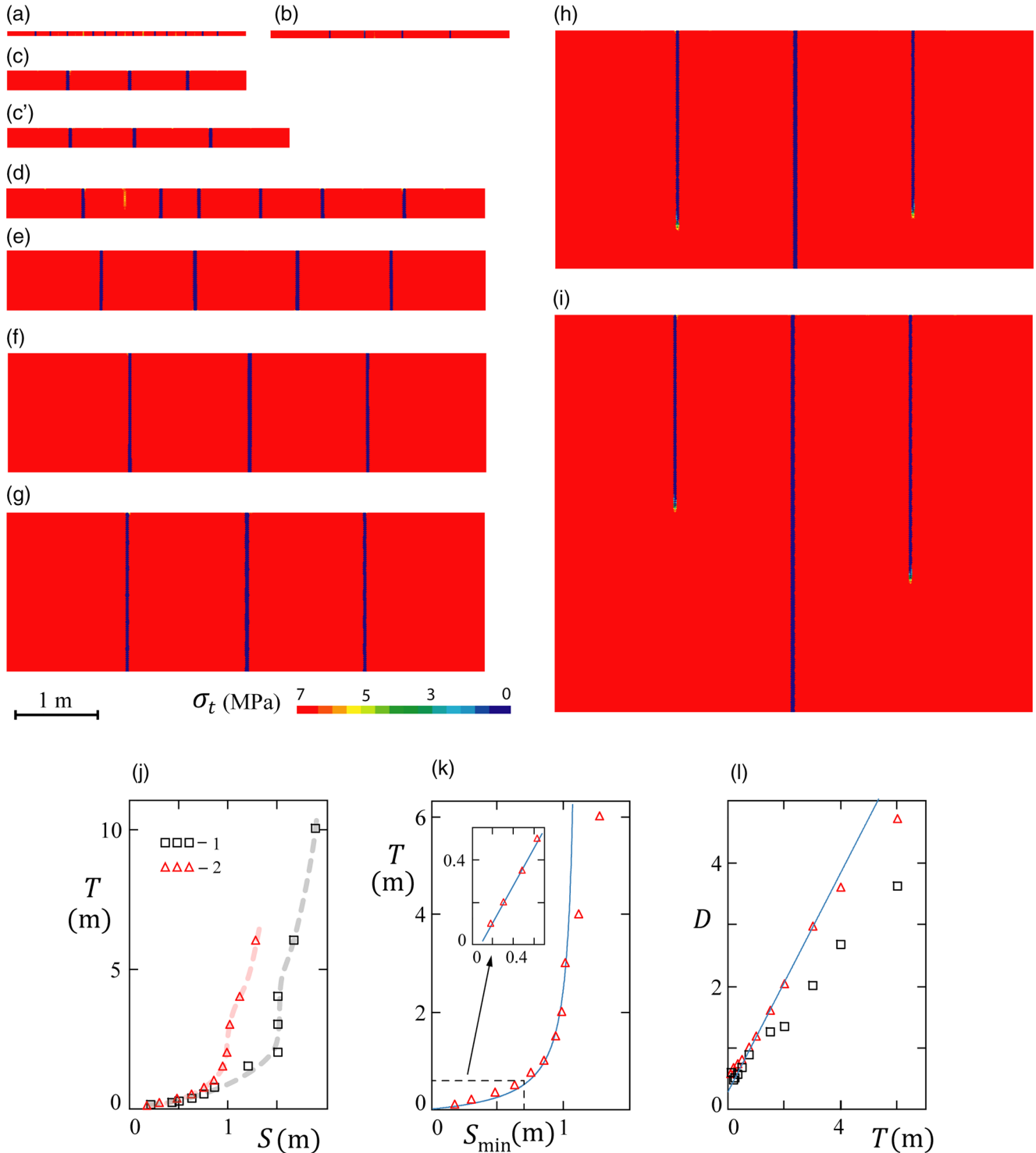
Figure 6. Group 4. (a–i) Fracture patterns in the models with different thickness T run to $\varepsilon_{xx} = -6 \times 10^{-3}$. T is 0.125, 0.2, 0.5, 0.75, 1.5, 3, 4, 6, and 10 meters in (a–i), respectively (note that the models presented are half-symmetry). The length L of the models is 3 m in (a–c), and 6 m in (d–i). In (c'), L=3.3 m and T=0.5 m as in (c). (j) Plots $T(S)$ obtained from numerical models. 1, Points (T, S_{av}) from the models shown in this figure, where S_{av} is the average over the model length fracture spacing; 2, Points (T, S_{min}) obtained in another set of models where L was progressively reduced until the fracture could not cut the entire layer thickness at $\varepsilon_{xx} = -6 \times 10^{-3}$. The minimum fracture spacing S_{min} was defined then as S_{min}=L/2. (k) Points (T, S_{min}) approximated by function T=$bS/(1-aS)$ from (Equation 17). The inset shows a zoom-in of the plot $T(S_{min})$ for small S_{min}. (l) the same points as in (j), but plotted in coordinates (D, T), are approximated by linear function D=$aT+b$, where coefficients a and b are the same as in (k): a=0.89 m^{-1} and b=0.27 m.
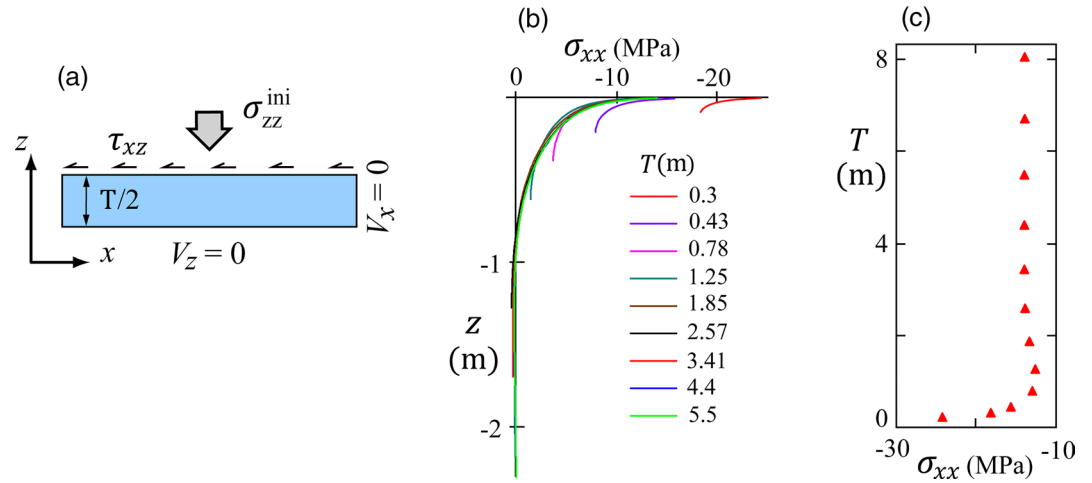
Figure 7. Group 5. One-layer elastic modeling. (a) Setup showing the layer (its quarter-symmetry model) deforming under shear (τ_{xz}) and normal (σ_{zz}^{ini}) stresses applied to the layer top. $\tau_{xz} = 2$ MPa is equal to the reference value of τ_0^i. $\sigma_{zz}^{ini} = 10$ MPa, the same as in previous models. The right vertical boundary of the layer is fixed in the x-direction, and the left boundary is free (i.e., corresponds to the preexisting fracture). A series of simulations have been carried out with the layer length $L=1$ m and different thicknesses $T/2$. (b) Vertical profiles of σ_{xx} along the right layer boundary for different T indicated in the figure. (c) σ_{xx} values at the right upper corner of the model plotted against T.

shadows' in b2', where the lower limit of $|\sigma_3|$ is increased to 4 MPa. Their presence is also reflected in the steps of $\tau^i(x)$ curve in Figures 3b4, 3c4, and 3d4. In Figure 3c, two fractures are formed and produce stress shadow in c2, and so on until the formation of six fractures in Figure 3f. In this figure $\varepsilon_{xx} = -5 \times 10^{-3}$, but the set of six fractures was already formed at $\varepsilon_{xx} = -1 \times 10^{-3}$ and does not change to $\varepsilon_{xx} = -2 \times 10^{-2}$ to which the models were run.

In Figure 3f4, the entire interface has been broken and repeatedly slipped at different deformation stages from a to f. Note that the fracture spacing S is not constant along the layer; one layer segment separated by fractures is clearly longer, but not long enough to accommodate one more fracture. Small modifications of any model parameter, for example, a slight increase in L, can lead to the reorganization of the fracture locations and increase (or on the contrary, reduce) their number, changing the average S value. This variability of S will be discussed below.

Group 2: Figure 4. The models of this group show the dependence of the fracture pattern on model resolution Δz and the setup. For the setup in Figure 4a (corresponding to Figure 2c), Δz increases by factor four
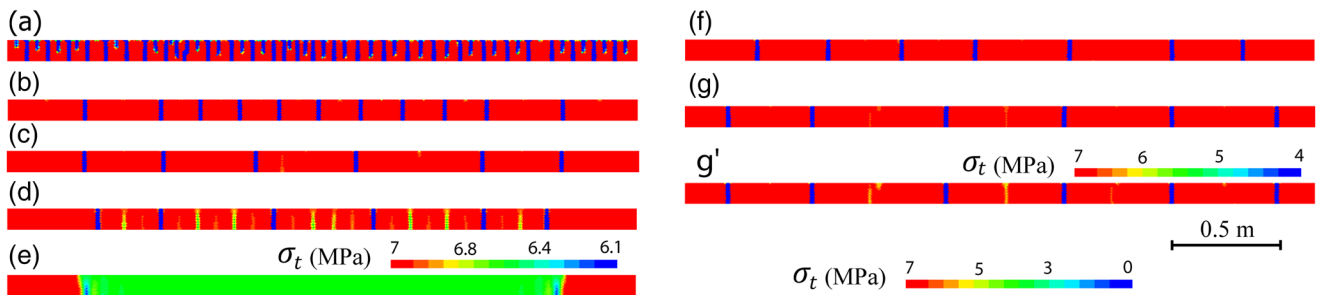

Figure 8. Group 6. (a–e) Models with reference parameters except C (from Equation 9) which varies for two orders of magnitude: in (a) $C=0.01$ m, in (b) $C=0.03$ m, in (c) $C=0.1$ m (the reference value), in (d) $C=0.3$ m, and in (e) $C=1$ m. (f and g) Models with reference parameters but different boundary conditions. In (f), a constant vertical stress $\sigma_{zz} = \sigma_{zz}^{ini}$ is applied directly to the top of the model instead of the velocity Vz in all previous models. In (g), a horizontal extension (velocity Vx) is applied to all three layers of the model instead of only the elastic layers in the previous models. (g') is the same as (g), but the lower limit of the σ_t color-scale is increased from 0 to 4 MPa. In (g' and e), color-scales are just above the models, and for all other cases, it is in the right lower part of the figure. All models were run to $\varepsilon_{xx} = -6 \times 10^{-3}$.

from 6.25×10^{-3} m in Figure 4b to the reference value of 2.5×10^{-2} m in Figure 4d. As expected, the fracture (band) width d increases linearly with Δz, but the fracture pattern changes little. In Figures 4b and 4c, there are six, and in Figure 4d, seven fractures formed. This small difference is due to the S variability indicated above, and which is also seen in Figures 4g and 4h showing models with the full layer thickness. Here the result is inverted; the model with smaller Δz contains seven fractures (Figure 4g) and that with higher, reference Δz value, six fractures (Figure 4h). Therefore, the conclusion is that the modeling results are not very sensitive to the model resolution (if it is not very small, smaller than the ones used in this work) or the setups in Figures 4a and 4f. Despite very different d_0 values, the average apparent fracture aperture Δl calculated as defined in (Chemenda, 2019) is close in the models in Figures 4b, 4c, and 4h with different Δz and the same fracture number: it is around 2 mm. This suggests that the mesh size has been appropriately integrated into the constitutive formulation in Equation 9. If this equation is ignored, the results are very different for different Δz (compare models in Figures 4d and 4e having the same resolution). In the model in Figure 4e, ε^0 is the same as in the model with smaller Δz in Figure 4b. One can see that in this case, a dense set of dilation bands is formed, and only some of them evolve to fractures.

Group 3: Figure 5. Here we investigate the impact of the interface shear strength τ_0^i on the fracture pattern. Figures 5a–5f show that this impact is strong and consists in the increase of D ($D=T/S_{av}$) with τ_0^i which ceases as the ratio τ_0^i / σ_t^0 approaches unity (Figure 5g). Similar fracture densification with the increase of the interface strength was obtained in Discrete Element Method models by Schöpfer et al. (2011). The interface slip also ceases as τ_0^i / σ_t^0 approaches to unity: in Figure 5f it occurs only within the fracture bands. Note that in this case (this figure), the upper part of the layer is strongly damaged, which leads to the τ^i reduction and explains the absence of plateaus in the $\tau^i(x)$ curve, which are seen in Figures 5a–5e.

Group 4: Figure 6. Here we vary T, with other parameters being equal to the reference values. The model length is $L = 3$ m for small T (Figures 6a–6c) and $L = 6$ in Figures 6d–6i. One can see that for relatively small T ($T<1.5$ m), S rapidly increases with T (Figures 6a–6f), but for larger T, S scarcely changes (Figures 6f–6i). In Figures 6h and 6i with $T = 6$ and 10 m, not all fractures cut through the entire layer thickness at the chosen ε_{xx} value of -6×10^{-3}. In Figure 6h, all the fractures completely cut the layer at $\varepsilon_{xx} = -6.3 \times 10^{-3}$ and in Figure 6i, at $\varepsilon_{xx} \approx -1 \times 10^{-2}$. The average fracture spacing S_{av} obtained from the images in Figures 6a–c and 6d–6i, is plotted against T in Figure 6j (black squares). For the cases when not all fractures cut through the entire layer thickness, S_{av} was calculated as

$$S_{av} = \frac{LT}{T + 2l}, \tag{16}$$

where l is the total length of the fractures formed in the half-thickness layer. This formula also is valid when all the fractures completely cut the model. The plot $T(S_{av})$ can be divided into two parts. The first one ($S_{av}<\sim1.5$ m) has a shallow dip, and the second ($S_{av}>1.5$ m) is very steep. In fact, one can distinguish the third segment at $S_{av}\approx1.5$ m, where the plot is practically vertical. The S_{av} values can vary in certain limits in the models with the same T but different L. This can be seen by comparing Figures 6c and 6c′ where T is the same, $T=0.5$ m. The explanation is that for a given set of model parameters, there exists a minimum S value, S_{min}. The spacing S between adjacent fractures can vary along the layer between S_{min} and $2S_{min}$ and thus is not constant. S_{min} characterizes a fracture set more objectively and the plot $T(S_{min})$ is physically more pertinent. To define S_{min} for different T, we run a series of models where L was progressively decreased under the same other conditions to define the minimum $L=2S_{min}$ value at which a single fracture cuts the layer completely. The corresponding points $T(S_{min})$ are plotted in Figure 6j (red triangles). Again, one can distinguish three segments with different dip. Both curves $T(S_{min})$ and $T(S_{av})$ are very close at relatively small T and deviate from each other with the T increase. Both curves are generally strongly nonlinear, but at relatively small T ($T<\sim50$ cm), they can be approximated by a straight line (inset in Figure 6k) quite satisfactorily. On the other hand, the relation $D(S)$ is much more linear (Figure 6l) particularly up to $T\sim3$ m. In this domain, the points $D(T)$ can be approximated by a straight line $D=aT+b$ (Figure 6i). As a consequence, the corresponding points in coordinates (T, S) are approximated by a nonlinear function

$$T = \frac{bS}{1 - aS} \tag{17}$$

(Figure 6k) with the same coefficients a and b, given in the caption of Figure 6.

At large T, the pure dilation deformation bands form only in the interfaces' vicinity, unlike the model in Figure 3a3, showing dilation bands cutting through the entire layer. The bands give way to the fractures propagating within the layer. The fracture aperture Δl is maximum in the vicinity of interfaces and increases during the fracture propagation. In the far-right fracture in Figure 6i, $\Delta l \approx 2$ mm near the layer top, and when the fracture tip reaches the layer bottom, $\Delta l \approx 5.2$ mm. This aperture progressively increases during the fracture propagation with the $\left| \varepsilon_{xx} \right|$ increase from 4.7×10^{-3} (when $\Delta l \approx 0$ and fracture is just initiated) to 9.5×10^{-3} when it reaches the layer bottom, which corresponds to the middle of the entire layer 2. Therefore, the fracture propagation is quasistatic contrary to the deformation banding (bifurcation), which is a dynamic phenomenon (Hill, 1962; Mandel, 1964). Note that the $\tau^i(x)$ profiles in all the models in Figure 6 have the same aspect as in Figure 3f4, corresponding to the extension of the models after their saturation with fractures.

More numerical simulations were conducted under the conditions of the models in Figure 6 but with different dilatancy coefficients β_c. In all presented models, $\beta_c = \beta_c^0 = 1$ in (8), which corresponds to zero dilatancy factor β, meaning that the dilatancy can occur only during the tensile failure. Two other cases discussed in Section 2, were tested as well as: $\beta_c^0 = \alpha_c$ in (8), and $\beta_c = \beta_c^0 = \alpha_c$. The latter case corresponds to an associated flow rule used in Chemenda (2019). The obtained fracture patterns were the same in all cases, which is not surprising as fracture initiation occurs in a tensile failure regime through the dilation banding when the shear failure mechanism is not yet activated. This mechanism is activated later within the bands during their evolution (Chemenda, 2019), that is, too late to affect the fracture pattern. On the other hand, β_c affects the rate of fracture growth. For example, the last fracture formed in the model in Figure 6f is the one furthest to the right. During its propagation through the entire layer thickness in this model, $\left| \varepsilon_{xx} \right|$ increased by 3.4×10^{-4}, in the model with $\beta_c^0 = \alpha_c$ in (8), this value is 7×10^{-5}, and for $\beta_c = \beta_c^0 = \alpha_c$, 4×10^{-5}. The dilatancy of the material within the fracture thus promotes fracture propagation. This parameter is part of a constitutive formulation for shear failure (Equations 1–4) and should have a much more substantial impact on shear fracturing.

Group 5: Figure 7. The models of this group were carried out to understand the cause of the steepening of the $T(S)$ curves in the range 1 m $< T <$ 2 m. One-layer elastic models were subjected to almost the same initial and boundary stresses as above shown in Figure 7a, including shear stress $\sigma_{xz} = 2$ MPa applied to the top of the layer to simulate the interfacial shear stress in the previous models. The maximum tension with this setup occurs at the right, fixed in the x-direction vertical boundary of the layer; this is the potential fracturing (failure) location. The left boundary corresponds to a preexisting fracture. Therefore, L has a sense of fracture spacing S in this quarter-symmetry model. We set L (or S) to 1 m which corresponds to $T \approx 2$ m in the $T(S_{\min})$ curve in Figure 6k and vary T in different models. The vertical profiles $\sigma_{xx}(z)$ along the right ends of these models are shown in Figure 7b for different T. As expected, $\left| \sigma_{xx} \right|$ is the largest at the model surface in all the cases and decreases with depth. At a relatively small T, the profiles are very different, but starting from $T \sim 2$m, they almost coincide although obviously continue to different depths $z = T/2$.

This "stabilization" of the stress is also seen in Figure 7c, showing σ_{xx} at the far-right point of the layer surface for different T. The absolute value of this stress rapidly decreases with T increase and reaches a minimum at $T \approx 1$ m that is very close to the L or S value in these models. It then slightly increases again and stabilizes at $T \sim 2$ m.

The stabilization (verticalization) of the $T(S)$ curves in Figure 6j occurs at approximatively the same T, $T \approx 2S \approx 2$ m. The geometry of the $T(S)$ (Figure 6k) and $T(\sigma_{xx})$ (Figure 7c) curves is similar as well, which makes understandable a rapid change of the slope of $T(S)$ curve at $T \approx 2S$ in the presented three-layer models: a stabilization of S at large T is due to the stabilization of the $\sigma_{xx}(z)$ profiles in the upper and lower parts of the layer, as is discussed below. Note that the slope of the curve in Figure 7c stabilizes at $\sigma_{xx} \approx -14$ MPa, which is more than twice σ_t^0 in magnitude. Such stresses are not reached in the elastoplastic models presented (where the maximum possible tensile stress is $-\sigma_t^0$) because of the inelastic deformation of the layer that starts well before the fracture initiation and is needed for this initiation to occur.

Group 6 includes auxiliary models showing the dependence of the fracture pattern on the parameter C (Figures 8a–8e) and on the boundary conditions applied to the vertical (Figure 8f) and horizontal (Figures

8g and 8g′) boundaries of the models. The *C* value is varied here for two orders of magnitude from 0.01 (in Figure 8a) to 1 m (in Figure 8e) with the reference value *C*=0.1 m (in Figure 8c) in the middle of this range. One can see that the average fracture spacing systematically increases from Figures 8a–8e with the increase of *C* or of the negative hardening modulus *h* from Equation 13. Less negative *h* corresponds to less brittle/more ductile material behavior. The critical *h* value, h_{cr}, for the tensile failure in the model (1–4) is zero. At this value, the spacing of the initiating deformation bands is theoretically infinite, and it should decrease with the *h* reduction (Chemenda, 2007, 2009). This is what is seen in Figures 8a–8c. In Figure 8a, *C* and hence *h* are the smallest; therefore, the material is the most brittle and fracture spacing is the smallest. The fractures initiate at the layer top, and many of them do not cut the entire layer thickness. In Figure 8e, *C* is the largest and *h* approaches zero. Therefore, deformation bands and hence fractures could not form. In the model in Figure 8d with *C*=0.3 m, there are many undeveloped fractures that are the dilation bands with a high degree of material damage, but they do not evolve to fractures. In this relatively ductile model, the bands and fractures were initiated within the layer′s body or in its lower part (corresponding to the middle of the entire layer 2 in Figure 2b) rather than at the top. The same result was obtained by Chemenda (2019).

In Figure 8f, a constant vertical stress $\sigma_{zz} = \sigma_{zz}^{\text{ini}}$ is applied to the top of the model instead of the velocity V_z in all other models (except those in Figure 7). Comparison of this model with the reference one in Figure 8c does not reveal any fundamental difference. Finally, the model in Figure 8g was conducted to appreciate the effect of the way the horizontal velocity V_x is applied to the model. In Figure 8g, V_x is applied to all three layers, leading to the model's uniform stressing up to the fracture initiation. In the reference model, where V_x is applied only to the elastic layers, the stress field is not uniform at all near the vertical ends of the model corresponding to the preexisting fractures, but it is practically uniform sufficiently far from the ends (Figure 3a2). One can see, that the maximum *S* value in Figure 8g is somewhat larger than in Figure 8c, but the number of the layer segments between the fractures is the same, 7. The longest layer segments in Figure 8g are not sufficiently long to form new fractures within them, but in Figure 8g′ with a different color scale, one can see that these fractures have already been initiated.

5. Concluding Discussion

The strongly nonlinear relation between fracture spacing *S* and thickness *T* (Figure 1d) of a fractured layer for *T*∼> 1 m known since detailed field measurements by McQuillan (1973) and Ladeira and Price (1981) is now reproduced in the numerical models (Figures 6j and 6k). At a relatively small *T* (*T* < ∼50 cm), this relation is close to the linear one (inset in Figure 6k), which is in line with the previous theoretical and numerical models, as well as numerous field studies mostly carried out on the *T* values within the indicated range. The complete *T*(*S*) curves includes this quasilinear shallow segment and much steeper segment at *T* > ∼ 1–1.5 m both in nature (Figure 1d) and the model (Figure 6j). Our results show that both segments of the *T*(*S*) curve are defined by the mechanical interaction between the layers. It is not necessary to involve external factors such as pore pressure gradient induced by fracture formation as suggested by Ladeira and Price (1981). The transition between the segments occurs when ratio *D*=*T*/*S* increases to a critical value D_{cr} of about 2, Figure 6k (note that *D* increases near-linearly with *T*, both in nature Figure 1e and model Figure 6l). The critical *T* and *S* values are therefore related as $T_{cr} \approx 2S_{cr}$. D_{cr} is reached when the horizontal normal stress σ_{xx} in the middle of the layer (at distance *z*=−*T*/2 from its top) becomes zero. The thickness of the central part of the layer with zero or slightly compressive σ_{xx} increases with the *T* > T_{cr} increase. Outside this part, σ_{xx} is tensile and $|\sigma_{xx}|$ increases toward the layer top and bottom, the profiles $\sigma_{xx}(z)$ being practically the same for any *T*>T_{cr} (Figure 7b). Therefore, if fracture cuts though the layer of thickness *T*=T_{cr}, it will also cut through the thicker layer at almost the same *S*. This is the reason why *S* stabilizes at large *T*. This stabilization is however not total in the models as the distance of the vertical propagation of fracture increases with *T* increase (this distance is simply equal to 0.5*T*). At depths > ∼1 m (*z*<∼−1 m in Figure 7b), the propagation occurs within the material with a slightly compressive background stress σ_{xx} and is quasistatic. A larger propagation distance (larger *T*) requires a larger extension of the adjacent layers or larger strain $|\varepsilon_{xx}|$. Since these layers are assumed to be elastic, the ε_{xx} value should be limited; otherwise, these layers will start deforming inelastically in natural conditions. In the models in Figure 6, ε_{xx} was arbi-

trarily limited to -6×10^{-3}, but without this limitation, all the fractures in Figure 6i cut through the entire layer thickness at larger ε_{xx}. There is only one way to make the fracture propagate to the bottom of a thicker layer with the limited ε_{xx}, to increase the distance between the existing fractures and hence, to increase S_{min}. That is why the vertical segments of the $T(S)$ curves in Figure 6j are followed by less steep segments at larger T. If the behavior of layers 1 and 3 (Figure 2a) were not purely elastic but included inelastic (plastic and/or viscous) component, there would be no limitations on ε_{xx}. The ductile horizontal extension of such layers could even occur without tension, under the differential stress if it is large enough compared to the layers' strength. Therefore, in future models, layers 1 and 3 should be allowed to deform inelastically, which will complicate the modeling and bring additional uncertainties, but which will make models more adequate as the available data suggest that shale layers can creep (e.g., Sone & Zoback, 2013) and undergo both shear and tensile fracturing (e.g., Gross & Eyal, 2007) seen in Figure 1a. The present, as well as the prior mechanical/modeling studies, show however that the elastic analysis in combination with more realistic constitutive models remains useful. It allows to deepen our understanding of natural fracturing without the excessive complication of modeling and its theoretical framework that would inevitably render the results less physically transparent.

Although it is difficult to precisely define the slope of $T(S)$ curves from the geological data, they suggest some inclination of the curve at large T (Figure 1d), which may correspond to function (17) plotted in Figures 1d and 6k. Ladeira and Price (1981) suggested that S can be assumed to be constant at large T. This is not contradicted by the results obtained. Indeed, the length of slowly propagated "underdeveloped" fractures in Figure 6i is about 2 m. Can such fractures be stable in natural conditions, given that they should be filled with fluid exerting pressure on their walls and degrading the material strength in stress concentration zones around the fracture tips? Probably not; there is for instance little doubt that introducing in the models a progressive reduction of the tensile strength in the tip zone of a fracture during its propagation will lead to the fracture cutting through the entire layer at smaller ε_{xx}. Reduction of the tensile strength with the increase in T (size effect) and chemically assisted fracturing (Laubach et al., 2019) will lead to the same result.

The impact of the thickness of the incompetent layers at different strength of the interfaces τ_0^i, of the lithostatic pressure and the elastic moduli values should be studied as well, although several tests performed with different moduli values did not show any significant influence on the results.

As indicated, the inelastic properties of all the layers should be taken into account in future studies. This could lead to new effects such as fracture clustering, even though this can also be caused by the variation of a degree of layer coupling, brittleness (defined by $\tilde{\varepsilon}^0$ or C, Figures 8a–8e) or of the strength τ_0^i of interfaces between the layers. This strength was shown to strongly affect both fracture nucleation and spacing (Figure 5). Relatively small τ_0^i, comparable to the tensile strength σ_t is sufficient to lock the layer interface. If $\tau_0^i > \sigma_t$, the adjacent beds will behave as one single thick layer. This layer can include many stratigraphic beds and correspond to a mechanical unit (Cooke & Underwood, 2001). Figure 1c shows an example of such a situation where adjacent thick limestone beds form a mechanical unit. The interfaces between such a type of beds often undergo pressure solution and become stylolite planes (Lamarche et al., 2012) with highly rough surfaces (Schmitbul et al., 2004) that ensure strong coupling between the beds. This is quite a typical situation for limestone-limestone and marl-limestone interfaces (Toussaint et al., 2018). Pressure solution is also known to enhance cementation/embrittlement locally (Fabricius & Borre, 2007; Rustichelli et al., 2012). It can occur relatively early during the burial (e.g., Bruna et al., 2019; Koehn et al., 2012; Lamarche et al., 2012) at a depth of a few hundred meters, mainly where sharp mechanical or depositional contrast exists. Such a contrast can also occur in siliciclastic deposits between the beds with different granulometry and may increase the layer coupling. Therefore, a detailed study of the bed interfaces in the field, cores, and laboratory can provide constraints on the interface strength for future modeling.

Data Availability Statement

Data were not used nor created for this research.

References

Bai, T., & Pollard, D. D. (2000). Closely spaced fractures in layered rocks: Initiation mechanism and propagation kinematics. *Journal of Structural Geology*, *22*(10), 1409–1425. https://doi.org/10.1016/S0191-8141(00)00062-6

Bažant, Z. P., & Oh, B. H. (1983). Crack band theory for fracture of concrete. *Matériaux et Construction*, *16*(3), 155–177.

Bogdanov, A. A. (1947). The intensity of cleavage as related to the thickness of beds. *Soviet Geology*, *16*, 102–104.

Bruna, P. O., Lavenu, A. P., Matonti, C., & Bertotti, G. (2019). Are stylolites fluid-flow efficient features? *Journal of Structural Geology*, *125*, 270–277. https://doi.org/10.1016/j.jsg.2018.05.018

Chang, C., Zoback, M. D., & Khaksar, A. (2006). Empirical relations between rock strength and physical properties in sedimentary rocks. *Journal of Petroleum Science and Engineering*, *51*(3–4), 223–237. https://doi.org/10.1016/j.petrol.2006.01.003

Chemenda, A. I. (2007). The formation of shear-band/fracture networks from a constitutive instability: Theory and numerical experiment. *Journal of Geophysical Research*, *112*(B11). https://doi.org/10.1029/2007JB005026

Chemenda, A. I. (2009). The formation of tabular compaction-band arrays: theoretical and numerical analysis. *Journal of the Mechanics and Physics of Solids*, *57*(5), 851–868. https://doi.org/10.1016/j.jmps.2009.01.007

Chemenda, A. I. (2019). Origin of regular networks of joints: Experimental constraints, theoretical background, and numerical modeling. *Journal of Geophysical Research: Solid Earth*, *124*(8), 9164–9181. https://doi.org/10.1029/2019JB017454

Chemenda, A. I., Nguyen, S. H., Petit, J. P., & Ambre, J. (2011a). Mode I cracking versus dilatancy banding: Experimental constraints on the mechanisms of extension fracturing. *Journal of Geophysical Research*, *116*(B4). https://doi.org/10.1029/2010JB008104

Chemenda, A. I., Nguyen, S. H., Petit, J. P., & Ambre, J. (2011b). Experimental evidences of transition from mode I cracking to dilatancy banding. *Comptes Rendus Mécanique*, *339*(4), 219–225. https://doi.org/10.1016/j.crme.2011.01.002

Cherepanov, G. P. (1997). On the origin of joints in sedimentary rocks. In B. L. Karihaloo, Y.-W. Mai, M. I. Ripley, & R. O. Ritchie (Eds.), *Advances in Fracture Research, Proceedings of the Ninth International Conference of Fracture*, (Vol. 4, pp. 1757–1766). Sydney, Australia.

Colmenares, L. B., & Zoback, M. D. (2002). A statistical evaluation of intact rock failure criteria constrained by polyaxial test data for five different rocks. *International Journal of Rock Mechanics and Mining Sciences*, *39*(6), 695–729. https://doi.org/10.1016/S1365-1609(02)00048-5

Cooke, M. L., & Underwood, C. A. (2001). Fracture termination and step-over at bedding interfaces due to frictional slip and interface opening. *Journal of Structural Geology*, *23*(2–3), 223–238. https://doi.org/10.1016/S0191-8141(00)00092-4

Engelder, T., Gross, M. R., & Pinkerton, P. (1997). Joint development in clastic rocks of the Elk Basin anticline, Montana-Wyoming. In T. Hoak, A. Klawitter, & P. Blomquist (Eds.), *Fractured Reservoirs: Characterization and Modeling. Guidebook* (pp. 1–18). Denver, Colorado: Rocky Mountain Association of Geologists.

Fabricius, I. L., & Borre, M. K. (2007). Stylolites, porosity, depositional texture, and silicates in chalk facies sediments. Ontong Java Plateau–Gorm and Tyra fields, North Sea. *Sedimentology*, *54*(1), 183–205. https://doi.org/10.1111/j.1365-3091.2006.00828.x

Fall, A., Eichhubl, P., Bodnar, R. J., Laubach, S. E., & Davis, J. S. (2015). Natural hydraulic fracturing of tight-gas sandstone reservoirs, Piceance Basin, Colorado. *Bulletin*, *127*(1–2), 61–75. https://doi.org/10.1130/B31021.1

Gross, M. R. (1993). The origin and spacing of cross joints: examples from the Monterey Formation, Santa Barbara Coastline, California. *Journal of Structural Geology*, *15*(6), 737–751. https://doi.org/10.1016/0191-8141(93)90059-J

Gross, M. R., & Eyal, Y. (2007). Throughgoing fractures in layered carbonate rocks. *Geological Society of America Bulletin*, *119*(11–12), 1387–1404. https://doi.org/10.1130/0016-7606(2007)119[1387:TFILCR]2.0.CO2

Gross, M. R., Fischer, M. P., Engelder, T., & Greenfield, R. J. (1995). Factors controlling joint spacing in interbedded sedimentary rocks: Integrating numerical models with field observations from the Monterey Formation. *Geological Society, London, Special Publications*, *92*(1), 215–233. https://doi.org/10.1144/GSL.SP.1995.092.01.12

Guo, L., Latham, J. P., & Xiang, J. (2017). A numerical study of fracture spacing and through-going fracture formation in layered rocks. *International Journal of Solids and Structures*, *110*, 44–57. https://doi.org/10.1016/j.ijsolstr.2017.02.004

Hill, R. (1962). Acceleration waves in solids. *Journal of the Mechanics and Physics of Solids*, *10*(1), 1–16. https://doi.org/10.1016/0022-5096(62)90024-8

Hobbs, D. W. (1967). The formation of tension joints in sedimentary rocks: An explanation. *Geological Magazine*, *104*(6), 550–556. https://doi.org/10.1017/S0016756800050226

Hoek, E., & Martin, C. D. (2014). Fracture initiation and propagation in intact rock—A review. *Journal of Rock Mechanics and Geotechnical Engineering*, *6*(4), 287–300. https://doi.org/10.1016/j.jrmge.2014.06.001

Huang, Q., & Angelier, J. (1989). Fracture spacing and its relation to bed thickness. *Geological Magazine*, *126*(4), 355–362. https://doi.org/10.1017/S0016756800006555

Itasca. (2013). *Fast Lagrangian analysis of continua in 3-dimensions, version 5.0, manual*. Minneapolis: Itasca.

Jain, A., Guzina, B. B., & Voller, V. R. (2007). Effects of overburden on joint spacing in layered rocks. *Journal of Structural Geology*, *29*(2), 288–297. https://doi.org/10.1016/j.jsg.2006.08.010

Ji, S., Zhu, Z., & Wang, Z. (1998). Relationship between joint spacing and bed thickness in sedimentary rocks: effects of interbed slip. *Geological Magazine*, *135*(5), 637–655. https://doi.org/10.1017/S0016756898001459

Koehn, D., Ebner, M., Renard, F., Toussaint, R., & Passchier, C. W. (2012). Modelling of stylolite geometries and stress scaling. *Earth and Planetary Science Letters*, *341*, 104–113. https://doi.org/10.1016/j.epsl.2012.04.046

La Bruna, V., Lamarche, J., Agosta, F., Rustichelli, A., Giuffrida, A., Salardon, R., & Marié, L. (2020). Structural diagenesis of shallow platform carbonates: Role of early embrittlement on fracture setting and distribution, case study of Monte Alpi (Southern Apennines, Italy). *Journal of Structural Geology*, *131*, 103940. https://doi.org/10.1016/j.jsg.2018.05.018

Ladeira, F. L., & Price, N. J. (1981). Relationship between fracture spacing and bed thickness. *Journal of Structural Geology*, *3*(2), 179–183. https://doi.org/10.1016/0191-8141(81)90013-4

Lamarche, J., Lavenu, A. P., Gauthier, B. D., Guglielmi, Y., & Jayet, O. (2012). Relationships between fracture patterns, geodynamics and mechanical stratigraphy in Carbonates (South-East Basin, France). *Tectonophysics*, *581*, 231–245. https://doi.org/10.1016/j.tecto.2012.06.042

Laubach, S. E., Lander, R. H., Criscenti, L. J., Anovitz, L. M., Urai, J. L., Pollyea, R. M., & Olson, J. E. (2019). The role of chemistry in fracture pattern development and opportunities to advance interpretations of geological materials. *Reviews of Geophysics*, *57*(3), 1065–1111. https://doi.org/10.1029/2019RG000671

Lavenu, A. P., & Lamarche, J. (2018). What controls diffuse fractures in platform carbonates? Insights from Provence (France) and Apulia (Italy). *Journal of Structural Geology*, *108*, 94–107. https://doi.org/10.1016/j.jsg.2017.05.011

Lavenu, A. P., Lamarche, J., Gallois, A., & Gauthier, B. D. (2013). Tectonic versus diagenetic origin of fractures in a naturally fractured carbonate reservoir analog (Nerthe anticline, southeastern France). *AAPG Bulletin*, *97*(12), 2207–2232. https://doi.org/10.1306/04041312225

Li, L. C., Tang, C. A., & Wang, S. Y. (2012). A numerical investigation of fracture infilling and spacing in layered rocks subjected to hydro-mechanical loading. *Rock Mechanics and Rock Engineering*, *45*(5), 753–765. https://doi.org/10.1007/s00603-011-0194-x

Mandel, J. (1964). Propagation des surfaces de discontinuité dans un milieu élastoplastique. In H. Kolsky, & W. Prager (Eds.,). *Stress waves in anelastic solids* (pp. 331–340). Berlin, Heidelberg: Springer.

Mas, D., & Chemenda, A. I. (2015). An experimentally constrained constitutive model for geomaterials with simple friction–dilatancy relation in brittle to ductile domains. *International Journal of Rock Mechanics and Mining Sciences*, *77*, 257–264. https://doi.org/10.1016/j.ijrmms.2015.04.013

Matonti, C., Guglielmi, Y., Viseur, S., Garambois, S., & Marié, L. (2017). P-wave velocity anisotropy related to sealed fractures reactivation tracing the structural diagenesis in carbonates. *Tectonophysics*, *705*, 80–92. https://doi.org/10.1016/j.tecto.2017.03.019

McQuillan, H. (1973). Small-scale fracture density in Asmari Formation of southwest Iran and its relation to bed thickness and structural setting. *AAPG Bulletin*, *57*(12), 2367–2385. https://doi.org/10.1306/83D9131C-16C7-11D7-8645000102C1865D

Mohammed, A., & Mahmood, W. (2021). Vipulanandan failure models to predict the tensile strength, compressive modulus, fracture toughness and ultimate shear strength of calcium rocks. *International Journal of Geotechnical Engineering*, *15*(2), 129–139. https://doi.org/10.1080/19386362.2018.1468663

Narr, W., & Suppe, J. (1991). Joint spacing in sedimentary rocks. *Journal of Structural Geology*, *13*(9), 1037–1048. https://doi.org/10.1016/0191-8141(91)90055-N

Parent, T., Domede, N., Sellier, A., & Mouatt, L. (2015). Mechanical characterization of limestone from sound velocity measurement. *International Journal of Rock Mechanics and Mining Sciences*, *79*, 149–156.

Pollard, D. D., & Aydin, A. (1988). Progress in understanding jointing over the past century. *Geological Society of America Bulletin*, *100*(8), 1181–1204. https://doi.org/10.1130/0016-7606(1988)100<1181:PIUJOT>2.3.CO;2

Prevost, J. H., & Loret, B. (1990). Dynamic strain localization in elasto-(visco-) plastic solids, part 2. Plane strain examples. *Computer Methods in Applied Mechanics and Engineering*, *83*(3), 275–294. https://doi.org/10.1016/0045-7825(90)90074-V

Price, N. J. (1966). *Fault and joint development: In brittle and semi-brittle rock*. Oxford, UK: Pergamon Press Ltd..

Price, N. J., & Cosgrove, J. W. (1990). *Analysis of geological structures*: Cambridge University Press.

Rice, J. R. (1976). The localization of plastic deformation. In W. T. Koiter (Ed.), Theoretical and applied mechanics (Proceedings of the 14th International Congress on Theoretical and Applied Mechanics, Vol. 1, pp. 207–220). Delft, The Netherlands: North-Holland Publishing Co.

Rudnicki, J. W., & Rice, J. R. (1975). Conditions for the localization of deformation in pressure-sensitive dilatant materials. *Journal of the Mechanics and Physics of Solids*, *23*(6), 371–394. https://doi.org/10.1016/0022-5096(75)90001-0

Rustichelli, A., Tondi, E., Agosta, F., Cilona, A., & Giorgioni, M. (2012). Development and distribution of bed-parallel compaction bands and pressure solution seams in carbonates (Bolognano Formation, Majella Mountain, Italy). *Journal of Structural Geology*, *37*, 181–199. https://doi.org/10.1016/j.jsg.2012.01.007

Rybacki, E., Meier, T., & Dresen, G. (2016). What controls the mechanical properties of shale rocks?–Part II: Brittleness. *Journal of Petroleum Science and Engineering*, *144*, 39–58. https://doi.org/10.1016/j.petrol.2016.02.022

Sagy, A., & Reches, Z. E. (2006). Joint intensity in layered rocks: The unsaturated, saturated, supersaturated, and clustered classes. *Israel Journal of Earth Sciences*, *55*(1), 33–42.

Schmittbuhl, J., Renard, F., Gratier, J. P., & Toussaint, R. (2004). Roughness of stylolites: Implications of 3D high resolution topography measurements. *Physical Review Letters*, *93*(23), 238501. https://doi.org/10.1103/PhysRevLett.93.238501

Schöpfer, M. P., Arslan, A., Walsh, J. J., & Childs, C. (2011). Reconciliation of contrasting theories for fracture spacing in layered rocks. *Journal of Structural Geology*, *33*(4), 551–565. https://doi.org/10.1016/j.jsg.2011.01.008

Shao, Z., Armaghani, D. J., Bejarbaneh, B. Y., Mu'azu, M. A., & Mohamad, E. T. (2019). Estimating the friction angle of black shale core specimens with hybrid-ANN approaches. *Measurement*, *145*, 744–755. https://doi.org/10.1016/j.measurement.2019.06.007

Sone, H., & Zoback, M. D. (2013). Mechanical properties of shale-gas reservoir rocks—Part 2: Ductile creep, brittle strength, and their relation to the elastic modulus. *Geophysics*, *78*(5), D393–D402.

Sulem, J., Vardoulakis, I., Papamichos, E., Oulahna, A., & Tronvoll, J. (1999). Elasto-plastic modelling of Red Wildmoor sandstone. *Mechanics of Cohesive-frictional Materials: An International Journal on Experiments, Modelling and Computation of Materials and Structures*, *4*(3), 215–245. https://doi.org/10.1002/(SICI)1099-1484199905)4:3<215::AID-CFM61>3.0.CO;2-8

Toussaint, R., Aharonov, E., Koehn, D., Gratier, J. P., Ebner, M., Baud, P., et al. (2018). Stylolites: A review. *Journal of Structural Geology*, *114*, 163–195. https://doi.org/10.1016/j.jsg.2018.05.003

Vajdova, V., Baud, P., & Wong, T. F. (2004). Compaction, dilatancy, and failure in porous carbonate rocks. *Journal of Geophysical Research*, *109*(B5). https://doi.org/10.1029/2003JB002508

Xu, H., Zhou, W., Xie, R., Da, L., Xiao, C., Shan, Y., & Zhang, H. (2016). 1 Characterization of rock mechanical properties using lab tests and numerical interpretation model of well logs. *Mathematical Problems in Engineering*, *2016*, 1–13. https://doi.org/10.1155/2016/5967159